Proceedings of the Thirty-sixth (2026) International Ocean and Polar Engineering Conference **www.isope.org**
Orlando, Florida, USA, May 31-June 5, 2026

ISBN 978-1-880653-72-2; ISSN 1098-6189

Study on the Characteristics of Air Layer for Air Layer Drag Reduction over a 2D Flat Plate Based on the Euler-Euler Method

Qidi Gao[1], Xiaosong Zhang[2], Jianhua Wang[1], Decheng Wan[1]*

[1]Computational Marine Hydrodynamics Lab (CMHL), School of Ocean and Civil Engineering,
Shanghai Jiao Tong University, Shanghai, China
[2]China Ship Scientific Research Center Shanghai Branch, Shanghai, China
[*]Corresponding author

ABSTRACT

Air layer drag reduction (ALDR) on a flat plate is studied numerically using the Euler–Euler method in OpenFOAM. A designed cavity with a wedge and a rectangular section facilitates air layer formation. Key factors, including cavity geometry, injection rate and location, and flow velocity, are analyzed for their impact on air layer thickness, interface stability, and drag reduction performance. Results confirm the effectiveness of Euler-Euler method in capturing two-phase flow dynamics, and reveal the relationship between the state of the air layer and various influencing factors, offering practical insights for ship applications.

KEY WORDS: Air layer drag reduction; numerical simulation; Euler-Euler method; flat plate; air layer characteristics

INTRODUCTION

In recent years, driven by the dual imperatives of global emission reduction and cost efficiency in the shipping industry, Air Layer Drag Reduction (ALDR) technology for ships has witnessed significant breakthroughs, progressing from academic research towards engineering application. It is now at a critical juncture of transitioning from laboratory and test vessel stages to large-scale commercial implementation. Owing to its advantages of high drag reduction rate, low energy consumption, and environmental friendliness (Wang, et al., 2022), ship ALDR technology holds considerable promise for widespread future adoption in maritime transport.

The concept of bubble drag reduction was first proposed by McCormick (1973) through electrolysis experiments on revolving bodies. Since then, extensive research on both bubble drag reduction and air layer drag reduction has been conducted, consistently confirming the effectiveness of ALDR technology in reducing ship frictional resistance. Nevertheless, the underlying drag reduction mechanisms remain challenging to elucidate due to the complex nature of the two-phase flow, involving intricate physical processes such as bubble deformation, coalescence, and breakup. Early investigations predominantly relied on physical model experiments, including studies on revolving bodies (Deutsch, et al., 1986; Clark, et al., 1991). These experiments demonstrated that air-liquid mixed flows could achieve drag reduction of up to 80% and suggested a potential correlation between drag reduction effectiveness and the air volume fraction within the mixed flow. To delve deeper into the ALDR mechanisms and identify key influencing factors, subsequent research increasingly employed flat plate test configurations. For instance, Moriguchi, et al. (2002) experimentally found that bubble size within the mixed flow had a limited impact on drag reduction, whereas inflow velocity and air injection rate were critical factors. Follow-up flat plate experiments, including those on large-scale plates (Kodama, et al., 2007) and plates under high Reynolds numbers (Winkel, et al., 2007 and Elbing, et al., 2011), further investigated ALDR. These studies yielded insights into phenomena such as changes in bubble flow regime, the relationship between drag reduction and air injection location, and potential drag reduction mechanisms. Regarding the drag reduction mechanisms of ALDR, several prevailing theories have been established. These include: the alteration of local frictional resistance due to changes in near-wall porosity in microbubble drag reduction (Takahashi, et al., 2003; Murai, et al., 2007)—analogous to how a ship's wetted surface area affects friction, the presence of microbubbles effectively reduces the wetted surface of a plate, thereby lowering frictional drag. Lvov (2005) attributed drag reduction to a decrease in effective viscosity within the boundary layer resulting from the reduced mixture density in air-liquid flows. Sindagi (2021) proposed that the slip phenomenon at the plate surface induced by microbubble flow leads to reduced frictional resistance. Gao (2023) through flat plate experiments, concluded that microbubbles suppress the development of turbulent flow over the plate, thereby diminishing turbulence-induced frictional drag. While a growing body of research has shed light on ALDR mechanisms from various perspectives, formulating a unified theory to describe its practical drag reduction principles remains challenging. This difficulty stems from the fact that ALDR encompasses diverse air-liquid flow regimes, including microbubble flow, intermittent air layers, continuous air layers, and transitions between bubbles and layers, highlighting the need for further in-depth investigation.

Most existing experiments focus on microbubble drag reduction, with relatively few studies dedicated to air layer drag reduction in its true sense. Research on air layer development processes and morphology is particularly scarce. This gap exists primarily because ALDR involves complex air-liquid two-phase flows, making experimental measurement

of key air layer characteristics—such as layer height and morphology—highly difficult. Furthermore, experimental reproducibility under identical conditions is often low, limiting the generalizability of findings. With advancements in numerical simulation technology, computational studies have become an ideal alternative for ALDR research. For numerical simulation of the air-liquid two-phase flow in ALDR, the algebraic Volume of Fluid (VOF) method is frequently employed due to its relatively low computational cost and high stability, making it suitable for flows with strong air-liquid stratification (Montazeri, et al., 2019 and 2020). Simulations of flat plates with bottom air cavities using VOF can resolve the water-air interface. However, the VOF method has limitations. The fluid volume fraction is a discontinuous scalar function, and its discontinuity introduces significant errors in derivative calculations. Consequently, the accuracy and physical fidelity of interface computation can be adversely affected by mesh resolution. Moreover, ALDR flow development involves numerous discrete bubbles undergoing deformation, coalescence, and breakup. Constructing interfaces for such microbubbles using VOF would require prohibitively fine meshes, rendering it impractical. An alternative approach is the Euler-Lagrange method, which solves the continuous phase in a Eulerian framework and tracks individual microbubbles as Lagrangian points. Zhang (2020) proposed a bubble coalescence and breakup model that integrates VOF and Lagrangian methods to identify these events. This hybrid approach allows for interface resolution via the VOF method in regions of continuous air layer flow while treating microbubbles using the Lagrangian method, enhancing accuracy in capturing air-liquid interactions during ALDR flow development. This method also enables computation of bubble swarm coalescence and breakup in drag reduction problems (Zhang, et al., 2021). Despite its advantages for microbubble drag reduction, the Euler-Lagrange method requires solving the motion of each discrete bubble as an individual particle, incurring substantial computational overhead and thus being unsuitable for large-scale ship model simulations. In contrast, the Euler-Euler method offers a more computationally efficient approach for ALDR problems as it does not require resolving individual bubble interfaces. Qin, et al. (2017) performed numerical simulations of bubble drag reduction over a flat plate structure using this method, accounting for interphase forces between the continuous and discrete phases, and reported favorable agreement with experimental results.
In summary, numerical simulation currently serves as a viable methodology for ALDR technology research. Given that the ALDR process involves discrete bubble flow, strongly stratified air-water interface flow, and the transition/evolution between air layers and bubbles, the present study adopts the Euler-Euler method for numerical simulation. To account for interphase forces between water and air, as well as phenomena like bubble coalescence and breakup under turbulent conditions, the Interfacial Area Transport Equation (IATE) approach is incorporated. Numerical simulations will be conducted on a 2D flat plate equipped with an air cavity generation structure. The study aims to investigate the effects of leading-edge wedge height, air injection location, and inflow velocity on air layer morphology. The findings are expected to contribute a theoretical foundation for the application of ship ALDR technology.

NUMERICAL METHODS

In this study, the Euler-Euler method as the numerical approach for solving two-phase flow is used. To simulate phenomena such as bubble coalescence, breakup, and liquid entrainment, the IATE (Interfacial Area Transport Equation) method is adopted. The numerical simulations are conducted using the open-source CFD platform OpenFOAM.

Euler-Euler Governing Equations

The governing equations of the Euler-Euler method include the continuity equation and the momentum equation, expressed as:

$$\frac{\partial(\alpha_\varphi \rho_\varphi)}{\partial t} + \nabla \cdot (\alpha_\varphi \rho_\varphi \boldsymbol{U}_\varphi) = 0 \tag{1}$$

$$\frac{\partial(\alpha_\varphi \rho_\varphi \boldsymbol{U}_\varphi)}{\partial t} + \nabla \cdot (\alpha_\varphi \rho_\varphi \boldsymbol{U}_\varphi \boldsymbol{U}_\varphi) = -\alpha_\varphi \nabla p + \nabla \cdot (\alpha_\varphi \boldsymbol{\tau}_\varphi) + \alpha_\varphi \rho_\varphi \boldsymbol{g} + \boldsymbol{F}_i \tag{2}$$

where the subscript φ in the formulas is used to distinguish a specific phase, representing the physical quantities of water and air respectively. α represents the phase fraction, ρ denotes the density, U stands for velocity, $\boldsymbol{\tau}_\varphi$ indicates the effective stress, $\boldsymbol{g}$ is the gravitational acceleration, and $\boldsymbol{F}_i$ denotes the interphase interaction force. The expression for $\boldsymbol{\tau}_\varphi$ can be expressed as:

$$\boldsymbol{\tau}_\varphi = -\boldsymbol{\nu}_{\varphi,\mathrm{eff}} \left[\nabla \boldsymbol{U}_\varphi + \nabla^{\mathrm{T}} \boldsymbol{U}_\varphi \right] + \frac{2}{3} \boldsymbol{\nu}_{\varphi,\mathrm{eff}} \nabla \cdot (\boldsymbol{U}_\varphi \cdot \boldsymbol{I}) \tag{3}$$

where the $-\boldsymbol{\nu}_{\varphi,\mathrm{eff}}$ denotes the effective viscosity. In practical calculations, it is typically expressed as the sum of the viscous stress and the Reynolds stress, where the Reynolds stress can be solved using an appropriate turbulence model. If the LES (Large Eddy Simulation) method is adopted, an eddy viscosity model can be applied to solve this term.
Where the $\boldsymbol{F}_i$ represents the interphase forces, which can be categorized into drag force $\boldsymbol{F}_d$, lift force $\boldsymbol{F}_l$, turbulent diffusion force $\boldsymbol{F}_t$, wall lubrication force $\boldsymbol{F}_w$, virtual mass force $\boldsymbol{F}_v$, et al. However, in this study, as the motion of individual microbubbles is not considered, the lift force and wall lubrication force are disregarded. The drag force is expressed as:

$$\boldsymbol{F}_d = \frac{3}{4} \rho_w \alpha_a C_d \frac{\rho_w}{d_a} \left| \boldsymbol{U}_w - \boldsymbol{U}_a \right| (\boldsymbol{U}_w - \boldsymbol{U}_a) \tag{4}$$

where ρ_w and α_a represent the density of water and the volume fraction of air, respectively. C_d denotes the drag coefficient of the bubbles; d_a is the bubble diameter; and $\boldsymbol{U}_w$ and $\boldsymbol{U}_a$ represent the velocities of water and air, respectively. C_d is calculated using the Schiller–Naumann model (Schiller, et al., 1935), expressed as follows:

$$C_d = \begin{cases} \frac{24}{Re}(1 + 0.15 Re^{0.687}), Re < 1000 \\ 0.44, Re \geq 1000 \end{cases} \tag{5}$$

where Re represents the Reynolds number of the spherical particle, calculated based on the particle's diameter.

IATE Equation

The Interfacial Area Transport Equation (IATE) is employed for calculation. Its expression is as follows:

$$\frac{\partial a_i}{\partial t} + \nabla \cdot (a_i \boldsymbol{v}_i) = \frac{2}{3} \left(\frac{a_i}{\alpha} \right) \left(\frac{\partial \alpha}{\partial t} + \nabla \cdot \alpha \boldsymbol{v}_g - \eta_{ph} \right) + \frac{1}{3\psi} \left(\frac{\alpha}{a_i} \right)^2 \sum_j R_j + \pi D_{bc}^2 R_{ph} \tag{6}$$

where, a_i denotes the interfacial area concentration, $\boldsymbol{v}_i$ represents the interfacial velocity, α stands for the phase fraction, and $\boldsymbol{v}_g$ represents the

air-phase velocity. η_{ph} denotes the rate of volume generated by nucleation per unit mixture volume. In the one-group interfacial area transport equation, ψ can be calculated as 1/36π. R_j accounts for bubble changes induced by interactions between the fluid and bubbles, D_{bc} is the critical bubble size, and R_{ph} represents changes due to phase transition, which are not considered in this context.
Three additional equations are employed to model the phenomena of turbulent breakup, random coalescence, and wake-induced coalescence of bubbles within the flow, which is given by Ishii (2005). Their expressions are as follows:

$$R_{TI} = C_{TI}\left(\frac{nu_t}{D_b}\right)\exp\left(-\frac{We_{cr}}{We}\right)\sqrt{1-\frac{We_{cr}}{We}} \quad (7)$$

$$R_{RC} = C_{RC}\left[\frac{n^2 u_t D_b^2}{\alpha_{\max^{1/3}}(\alpha_{\max^{1/3}}-\alpha^{1/3})}\right]\times\left[1-\exp\left(-C\frac{\alpha_{\max^{1/3}}\alpha^{1/3}}{\alpha_{\max^{1/3}}-\alpha^{1/3}}\right)\right] \quad (8)$$

$$R_{WE} = C_{WE}C_D^{1/3}(D_b)n^2D_b^2u_r(D_b) \quad (9)$$

where the C_{TI} is a coefficient determined experimentally, D_b is the bubble diameter, and We_{cr} is the critical Weber number. In the second equation, C_{RC} and C are coalescence coefficients derived from experiments, and $\alpha_{\max}$ denotes the maximum packing limit. In the third equation, C_{WE} represents the coalescence coefficient determined experimentally, and C_D denotes the drag coefficient.

Turbulence Model

In this study, the k–ω SST turbulence model is adopted for the flow of gases and liquids. The transport equations for turbulent kinetic energy and specific turbulence dissipation rate are presented in differential form (Menter, 1994) as follows:

$$\frac{\partial\rho k}{\partial t}+\frac{\partial}{\partial x_j}\left(\rho v_j k\right)=\frac{\partial}{\partial x_j}\left[\left(\mu_L+\sigma_K\mu_T\right)\frac{\partial k}{\partial x_j}\right]+\tau_{ij}^F S_{ij}-\beta^*\rho\omega k \quad (10)$$

$$\frac{\partial\rho\omega}{\partial t}+\frac{\partial}{\partial x_j}\left(\rho v_j\omega\right)=\frac{\partial}{\partial x_j}\left[\left(\mu_L+\sigma_\omega\mu_T\right)\frac{\partial\omega}{\partial x_j}\right]+\frac{C_\omega\rho}{\mu_T}\tau_{ij}^F S_{ij} -\beta\rho\omega^2+2\left(1-f_1\right)\frac{\rho\sigma_{\omega2}}{\omega}\frac{\partial k}{\partial x_j}\frac{\partial\omega}{\partial x_j} \quad (11)$$

The equation for the Favre-averaged turbulent stresses τ_{ij}^F is as follows:

$$\tau_{ij}^F=-\overline{\rho}\,\widetilde{v_i''v_j''}=2\mu_T\tilde{S}_{ij}-\left(\frac{2\mu_T}{3}\right)\frac{\partial v_k}{\partial x_k}\delta_{ij}-\frac{2}{3}\bar{\rho}\tilde{k}\delta_{ij} \quad (12)$$

Where $\tilde{S}_{ij}$ and $\tilde{k}$ are the Favre-averaged strain rate and turbulent kinetic energy.

$$\mu_T=\frac{a_1\rho k}{\max\left(a_1\omega, f_2\|\operatorname{curl}\vec{v}\|_2\right)} \quad (13)$$

The above definition of the turbulent viscosity guarantees that in an adverse pressure gradient boundary layer, where the production of k is larger than its dissipation ω (hence $a_1\omega<\|\operatorname{curl}\vec{v}\|_2$, Bradshaw's assumption, that is, $\tau=a_1\rho k$ (shear stress proportional to turbulent kinetic energy) is satisfied. The function f_1, which blends the model coefficients of the $k-\omega$ model in boundary layers is defined as：

$$f_1=\tanh\left(aq_1^4\right) \quad (14)$$

$$aq_1=\min\left[\max\left(\frac{\sqrt{k}}{0.09\omega d},\frac{500\mu_L}{\rho\omega d^2}\right),\frac{4\rho\sigma_{\omega2}k}{CD_{k\omega}d^2}\right] \quad (15)$$

where d stands for the distance to the nearest wall and $CD_{k\omega}$ is the positive part of the cross-diffusion term, that is:

$$CD_{k\omega}=\max\left(2\frac{\rho\sigma_{\omega2}}{\omega}\frac{\partial k}{\partial x_j}\frac{\partial\omega}{\partial x_j},10^{-20}\right) \quad (16)$$

The auxiliary function f_2 is given by:

$$f_2=\tanh\left(a\varphi_2^2\right) \quad (17)$$

$$a\varphi_2=\max\left(\frac{2\sqrt{k}}{0.09\omega d},\frac{500\mu_L}{\rho\omega d^2}\right) \quad (18)$$

The model constants are: a_1=0.31, β*=0.09, κ=0.41. the coefficients of the inner model (k-w) are given by: σ_{kI}=0.85, $\sigma_{\omega I}$=0.5, β_I=0.075, $C_{\omega I}$=0.533.

NUMERICAL SIMULATION

Plate Model

The flat-plate model employed in this study incorporates a bottom cavity structure, as illustrated in Figure 1. The x-axis aligns with the flow direction, and the z-axis is perpendicular to the xy-plane and points upward, opposite to the direction of gravity. Since a two-dimensional problem is considered, no mesh is generated in the y-direction, and its wall type is specified as empty. A uniform inlet boundary condition is applied to the left side of the computational domain, with water as the only phase at the inlet. The bottom boundary is defined as a symmetry plane, the right boundary as an outlet, and the top boundary as a no-slip wall corresponding to the flat plate. The depth H of the computational domain is 0.3 m, and the total length of the flat plate is 1.67 m.

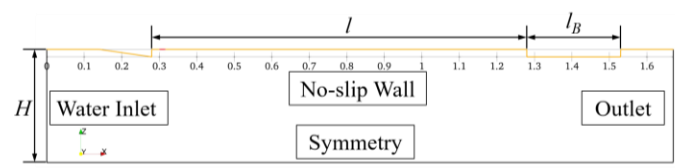

(a) Flat plate and computational domain

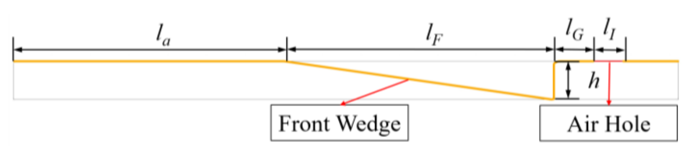

(b) Front wedge and air injection hole
Figure 1. Flat-plate model and computational domain setup.

The air injection hole is located at the front of the cavity, with a width l_I.

The influence of the injection hole size and air flow rate is not considered in this study; therefore, a fixed hole width and a fixed air injection velocity U_a are used across all cases. The distance from the front edge of the injection hole to the trailing edge of the front wedge is denoted l_G, which is analyzed as a variable. The height of the front wedge h is crucial for the air layer morphology within the cavity and is also treated as a variable. Additionally, the effect of different incoming flow velocities U_w on the air layer morphology is investigated. The cavity length L is 1 m, and the back block has a height of 0.02 m and a width l_B of 0.25 m. Four different water flow velocities U_w ranging from 0.7 to 1.0 m/s are simulated. The specific parameters are listed in Table 1.

Table 1. Parameters for the flat-plate numerical simulations.

Parameter	Meaning	Value
l	Length of the cavity	1 m
H	Height of domain	0.3 m
l_B	Width of Back block	0.25 m
l_a	Distance between inlet and front wedge	0.14 m
l_F	Length of front wedge	0.14 m
l_G	Distance between air hole and front wedge	0.02-0.36m
l_I	Width of air hole	0.015
h	Height of front wedge	0.01-0.04 m
U_w	Water flow velocity	0.7-1.0 m/s
U_a	air flow velocity	0.3 m/s

This study primarily focuses on the influence of three variables on the air layer morphology within the cavity: the water flow velocity U_w, the front wedge height h, and the air injection hole location l_G. To analyze the combined effect of different hole locations and wedge heights, the hole location is dimensionless as the ratio to the wedge height, i.e., $\Delta d = l_G/h$. The resulting case matrix for the numerical simulations is presented in Table 2.

Table 2. Numerical simulation cases

U_w (m/s)	h (m)	Δd
0.7, 0.8, 0.9, 1	0.01, 0.02, 0.03, 0.04	1, 3, 6,9

Grids Distribution

The mesh for the 2D flat plate is shown in Figure 2. Refinement is applied primarily around the plate and inside the cavity. The thickness of the refinement zone perpendicular to the plate is three times the cavity depth, aimed at resolving the flow within the air layer and the water-air interface.

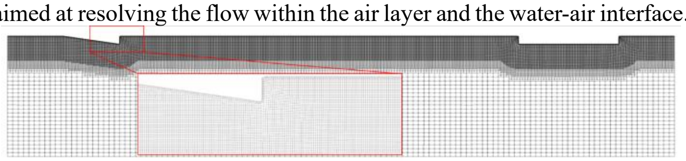

Figure 2. Mesh for the 2D flat-plate numerical simulation.

The morphology of the water-air interface is sensitive to grid resolution. Therefore, a grid independence study was conducted for both the streamwise (x) and wall-normal (z) directions, also considering the effect of the grid aspect ratio. Three grid sizes were tested in each direction, normalized by the front wedge height h, resulting in $\Delta x/h$=0.05, 0.1, 0.2 and $\Delta z/h$=0.05, 0.1, 0.2. The final results are summarized in Table 3.

Table 3. Comparison of water-air interface calculation results under different grid arrangements

	$\Delta x/h$=0.05	$\Delta x/h$=0.1	$\Delta x/h$=0.2
$\Delta z/h$=0.05	Interface oscillation	Interface smoothness	Interface smoothness
$\Delta z/h$=0.1	Interface oscillation	Interface minor oscillation	Interface smoothness
$\Delta z/h$=0.2	Non-physical	Non-physical	Interface smoothness

As shown in Table 3, non-physical results were obtained when the grid was coarse in the z-direction and the aspect ratio $\Delta x/\Delta z$ was small as shown in Figure 3(a), where the air layer adheres to the cavity wall forming a bulge, which is unphysical. With a moderate z-direction resolution but a small aspect ratio, the air layer morphology can be simulated, but the interface exhibits oscillation, as seen in Figure 3(b). A smooth and physically reasonable interface morphology was achieved with an aspect ratio $\Delta x/\Delta z \approx 2$ and a sufficiently fine grid in the wall-normal direction (at least 10 cells within the front wedge height h. Consequently, for all subsequent simulations, a grid with $\Delta x/\Delta z \approx 2$ and a minimum of 10 cells across the height h is adopted.

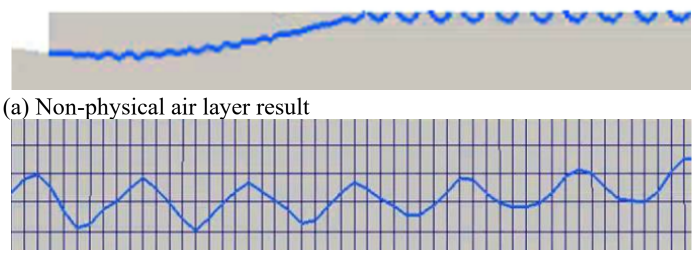

(a) Non-physical air layer result

(b) Oscillating air layer interface

Figure 3. Erroneous calculation results due to inappropriate grid arrangements

RESULTS AND DISCUSSION

Water-air Interface Fluctuation

Figure 4 illustrates the development process of the air layer in the numerical simulation under the conditions of h=0.02 m, U_w=0.7 m/s, and U_a=0.3 m/s with Δd=1. After air injection into the flow field, it initially resides in the low-pressure region behind the front wedge before gradually developing downstream. At a physical time of approximately t=2 s, the air covers the entire cavity plate, albeit with a thin thickness. By t=4 s, the waveform of the air-water interface has preliminarily formed, with only minor mixing disturbances near the back block. In subsequent simulations, the wavelength of the air layer changes minimally, but its thickness varies continuously, initially increasing and then decreasing until stabilizing around t=20 s.
From Figure 4, it can be observed that during an intermediate phase of air layer development (around t=8 s), a relatively thick air layer state with pronounced wave characteristics forms. However, due to further accumulation of the air layer, excessive air within the cavity leads to instability, causing slight breaking of the leading wave of the air layer. This subsequently affects the stability of the air-water interface,

preventing further accumulation of the air layer. Consequently, during subsequent development, a trend emerges where the air layer thickness decreases and wave characteristics weaken, eventually reaching a relatively stable air layer state (t=16 s, 20 s). Multi-condition simulations reveal that after a stable air layer forms within the cavity, instability does not occur at the rear but rather at a specific position upstream of the cavity, resulting in rupture or regions devoid of air. The cause of this phenomenon is the excessive height of the first wave behind the front wedge, which elevates the air-water interface and causes it to contact the solid wall boundary of the plate. This further reduces the stability of the air layer in that region. In contrast, the wave height downstream decreases significantly, preventing wave breaking and thus maintaining relatively higher stability.

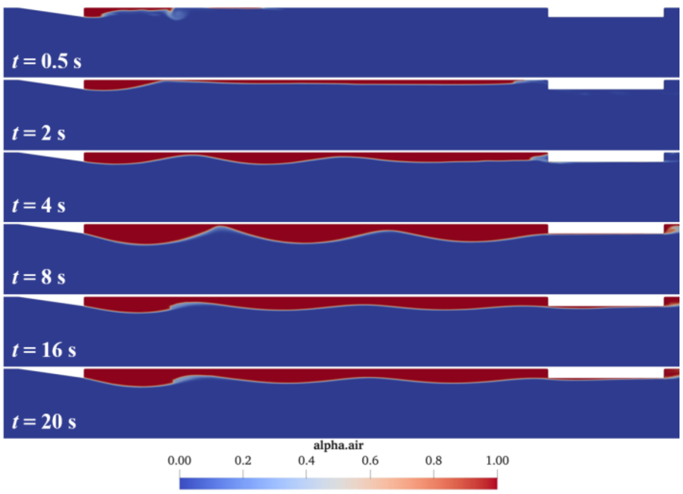

Figure 4. Two-dimensional development process of the air layer.

By investigating the transient flow field, the reasons for the wave characteristics of the air-water interface are further analyzed. Figure 5(a) shows the flow field near the first wave behind the front wedge after the air layer is fully developed. The streamlines indicate a significant difference between the flow states inside and outside the air layer. The liquid flow outside the air layer is relatively smooth, primarily in the streamwise direction. Inside the air layer, an elliptical vortex structure forms, characterized by counterclockwise motion. This elliptical vortex significantly influences the air layer surface, particularly the morphology of the first wave. When the vortex rotates intensely, the flow velocity perpendicular to the wall elevates the air-water interface, increasing the peak height on the right side of the vortex. Conversely, driven by the vortex, the air-water interface may roll over or experience interface breaking, entraining liquid from the external flow field into the air layer. This leads to air-water mixing at that location, increasing the likelihood of air layer disruption.

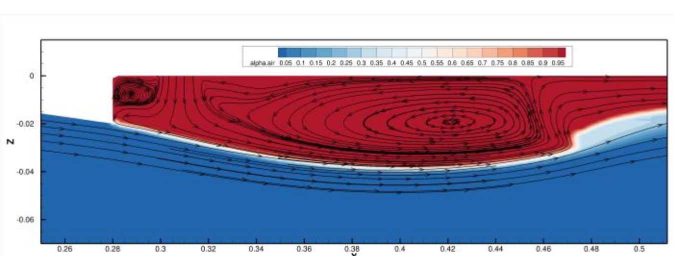
(a) Streamlines behind the front wedge.

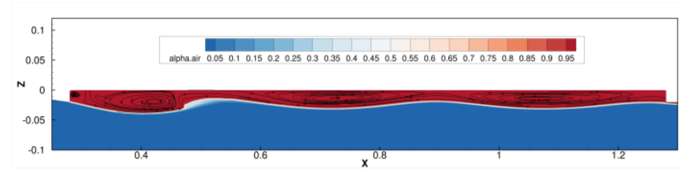
(b) Overall streamlines within the air layer.

Figure 5. Streamlines within the plate air layer.

Figure 5(b) depicts the overall flow state within the plate cavity. Under these conditions, three wave peaks are observed. Analyzing the streamlines within each peak reveals that the vortex inside the first wave is stronger than those inside the two downstream waves, manifested as a larger vortex size in the direction perpendicular to the wall. This phenomenon increases the elevation level of the air-water interface, resulting in higher wave heights. The primary cause of the first vortex is the effect of the front wedge. The rear-step vortex formed by flow around the step is an inherent phenomenon; it exists even in the absence of air and plays a crucial role in subsequent air injection, waveform air layer formation, and air-water interface stability.

Factors Influencing the Air-Water Interface

In gas layer drag reduction technology, numerous factors influence the gas layer, such as incoming flow velocity and gas injection velocity. This study focuses on factors affecting gas layer morphology, primarily considering the effects of incoming flow velocity, front wedge height, and gas injection location. The gas injection rate or velocity is kept at a relatively high constant value in this study to ensure gas layer formation across different conditions. To compare the effects of different conditions on the gas layer, quantitative comparison of waveforms is necessary. Dimensionless average wave height H_a, average gas layer thickness T_a, and average wavelength λ_a are defined as follows:

$$H_a = \frac{(D_1^t + D_2^t + \ldots + D_n^t) - (D_1^p + D_2^p + \ldots + D_n^p)}{n \cdot h} \tag{19}$$

$$T_a = \frac{(D_1^t + D_2^t + \ldots + D_n^t) + (D_1^p + D_2^p + \ldots + D_n^p)}{2n \cdot h} \tag{20}$$

$$\lambda_a = \frac{\lambda_1 + \lambda_2 + \ldots + \lambda_n}{n \cdot \mathrm{L}} \tag{21}$$

where D_i^t is the vertical distance between the i-th wave trough of the air-water interface and the plate surface, D_i^p is the vertical distance between the i-th wave peak and the plate surface, and λ_i is the wavelength of the i-th wave, and the n represents the number of waves.

First, the influence of different incoming flow velocities on the wave characteristics of the air-water interface is considered. Analysis is performed for the plate configuration with h=0.02 m and Δd=1. Figure 6 shows the morphology of the air-water interface after stable air layer development under different incoming flow velocities. The computational results indicate that incoming flow velocity strongly affects the air layer, particularly its wave characteristics. As the incoming flow velocity increases, the number of wave peaks decreases, accompanied by an increase in the wavelength of individual waves. The maximum height of the leading wave peak occurs at U_w=0.9 m/s; further increase in velocity results in a decrease in wave peak height.

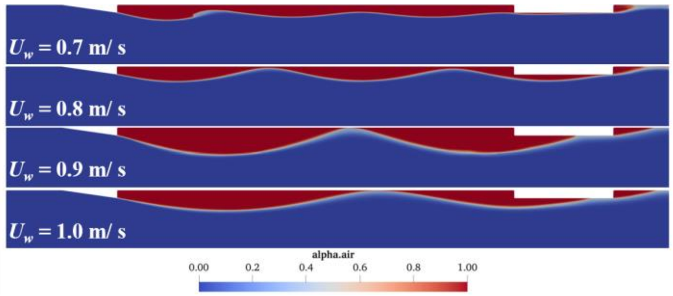

Figure 6. Air-water interface of the air layer under different incoming flow velocities for h=0.02 m, Δd=1.

Figure 7(a) shows a comparison of the dimensionless average wave height and maximum wave height, where the maximum wave height is selected as the height of the first wave peak within the air layer. The results indicate that the average wave height within the air layer initially increases and then decreases with increasing incoming flow velocity. The maximum average wave height is achieved at an incoming flow velocity of 0.9 m/s. Figure 7(b) shows the average thickness of the air layer. The results reveal an alternating trend in average thickness, but the maximum air layer thickness still occurs at a flow velocity of 0.9 m/s. Figure 7(c) shows the average wavelength within the air layer. The results indicate that the average wavelength increases monotonically with increasing incoming flow velocity.

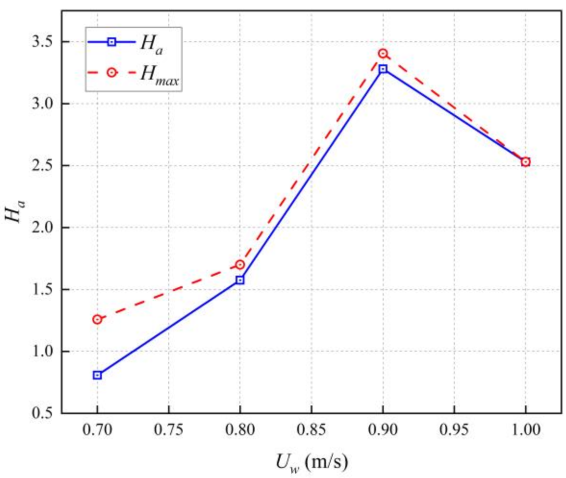

(a) Average and maximum wave height of the air layer.

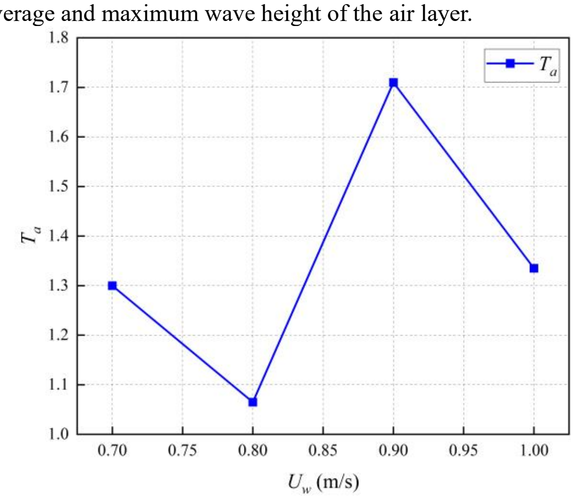

(b) Average thickness of the air layer.

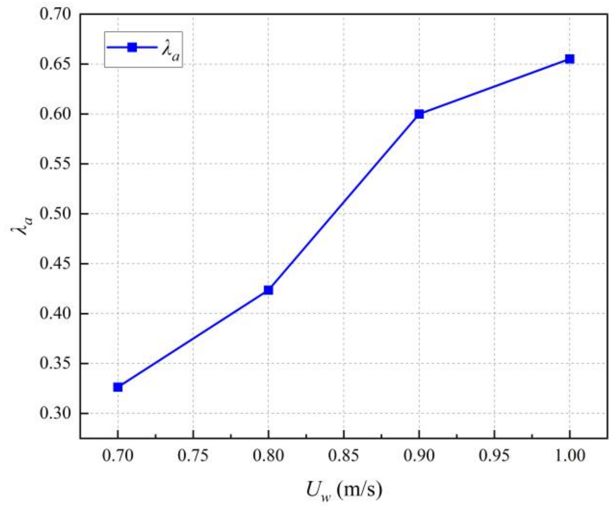

(c) Average wavelength of the air layer.

Figure 7. Dimensionless calculation results of wave characteristics within the air layer under different U_w for h=0.02 m, Δd=1.

From these three dimensionless results, it is evident that for a front wedge height of 0.02 m, the wave characteristics of the air layer do not change linearly with increasing incoming flow velocity but rather exhibit an optimal range for air layer morphology. Around an incoming flow velocity of 0.9 m/s, both the average wave height and average thickness of the air layer reach their maximum values. Combining this with the air layer morphology in Figure 6, it is found that at this condition, the air layer contains approximately two wave peaks with relatively high heights, resulting in the calculated maximum average thickness. When the incoming flow velocity is low, the air-water interface cannot generate large wave heights and flows in a form nearly flush with the front wedge height, leading to a lower average thickness. Notably, for h=0.01 m and 0.03 m, gradually increasing the incoming flow velocity without changing the air injection rate yields similar wave characteristics: the average wave height of the air layer peaks at an incoming flow velocity of 0.9 m/s and decreases at velocities below or above this value. However, when h further increases to 0.04 m, the situation changes: the maximum average wave height and average thickness occur at an incoming flow velocity of 1 m/s. This result indicates that the average wave height and average thickness of the air layer are jointly determined by the front wedge height and the incoming flow velocity, not by a single variable alone.

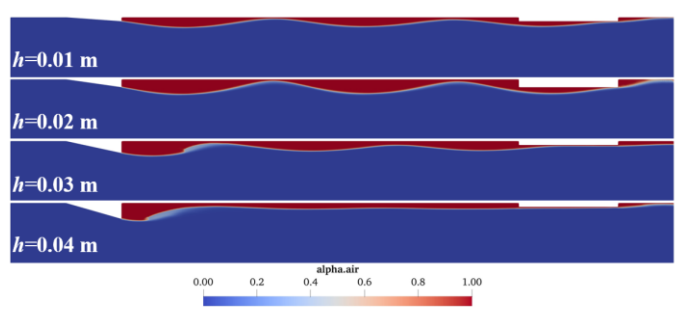

Figure 8. Air layer morphology under different h for Uw=0.8 m/s, Δd=1.

Next, the front wedge height h is investigated. Figure 8 shows the final air layer morphology under different h values for U_w =0.8 m/s and Δd=1. The results show that with a constant incoming flow velocity, the most apparent feature with increasing h is the gradual disappearance of wave characteristics in the air layer. At h=0.04 m, a complete wave no longer exists within the cavity; instead, it becomes a thin air layer almost parallel to the plate, with a thickness approximately equal to the height of the back block. At h=0.03 m, wave characteristics are basically present, but the trailing edge of the first wave shows signs of impending breaking, indicating more intense flow perpendicular to the wall in this region, making it difficult to maintain stable wave features.

Figure 9 shows the average wave height and average air layer thickness under different h conditions for U_w=0.8 m/s and Δd=1. Since obvious wave characteristics are absent at h=0.04 m, the thickness of the air-water interface within the cavity is taken as the average wave height and air layer thickness. Additionally, due to changes in the front wedge height, when calculating average wave height, air layer thickness, and average wavelength, h is taken as the average of the four heights, i.e., 0.025 m.

The results indicate that under the same incoming flow velocity, the average wave height of the air layer does not change linearly with increasing h but exhibits a clear maximum. In this study, the maximum average wave height forms at h=0.02 m. Simultaneously, when the average wave height within the air layer is larger, the corresponding average air layer thickness is also greater.

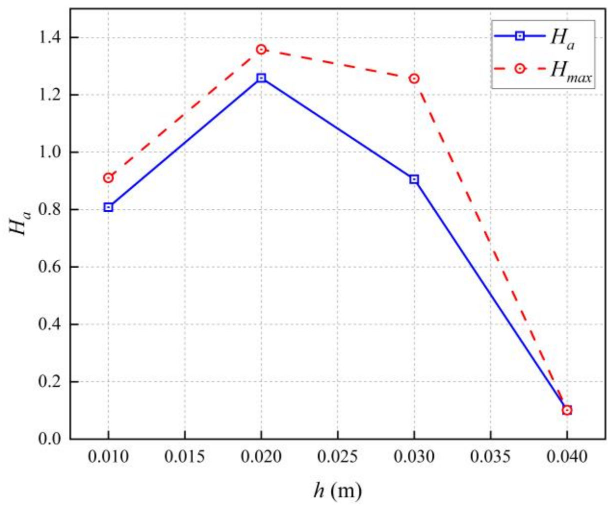

(a) Average and maximum wave height of the air layer.

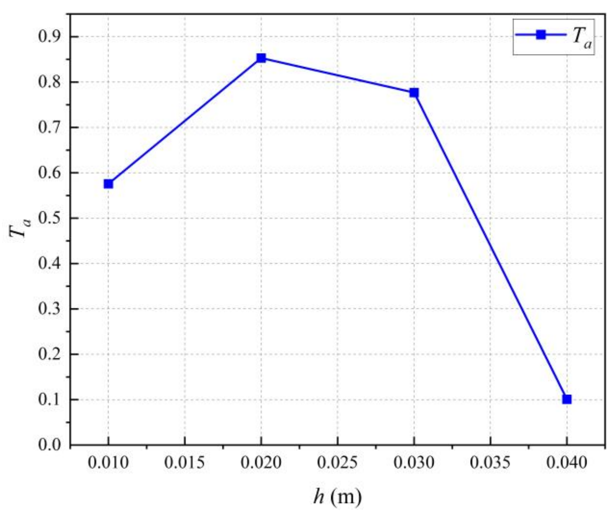

(b) Average thickness of the air layer.

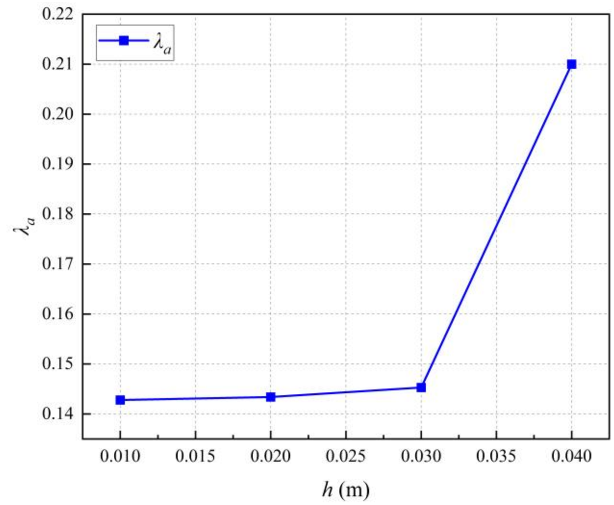

(c) Average wavelength of the air layer.

Figure 9. Dimensionless calculation results of wave characteristics within the air layer under different h for U_w=0.8 m/s, Δd=1.

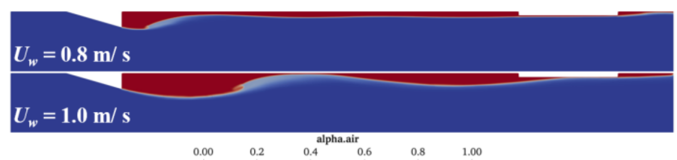

Figure 10. Comparison of air layer wave characteristics under different U_w for h=0.04 m, Δd=1.

However, when h is too large, a lower incoming flow velocity is insufficient to form wave characteristics in the air layer, resulting in a relatively flat interface stratification within the cavity—a flow state with very long wavelength and very small wave height. Further increasing the incoming flow velocity can then generate wave phenomena. This indicates that whether waves form at the air-water interface within the air layer is directly related to the front wedge height h and the incoming flow velocity Uw. Larger h requires a correspondingly larger Uw to form distinct wave characteristics, as shown in Figure 10.

Through the above comparisons of different incoming flow velocities U_w and different front wedge heights h, it is found that among the several conditions designed in this study, the highest average wave height and thickest air layer thickness are consistently obtained at h=0.02 m, indicating that stable wave characteristics of the air-water interface are more easily formed at this h. Next, the influence of different Δd on air layer morphology for h=0.02 m and Uw=0.7 m/s is investigated, as shown in Figure 11. The computational results reveal that under these conditions, changing Δd has almost no effect on air layer morphology, suggesting that the morphology of the air layer within the cavity is minimally influenced by different air injection locations under these conditions and is primarily affected by the incoming flow velocity. Comparisons of results for other h and corresponding U_w yield similar conclusions. Therefore, it can be inferred that the morphology of the air layer within the cavity is primarily and directly related to the front wedge height and the corresponding incoming flow velocity, while the air injection location has little influence.

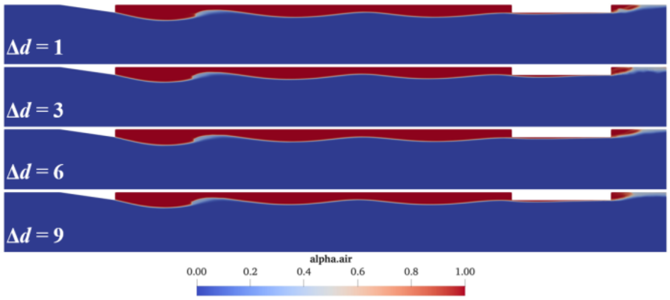

Figure 11. Comparison of air layer wave characteristics under different Δd for h=0.02 m, U_w=0.7 m/s.

CONCLUSIONS

This paper primarily conducts a numerical simulation study on the wave characteristics of the air layer in two-dimensional plate air layer drag reduction. Using the OpenFOAM platform, the Euler-Euler two-fluid method combined with the IATE (Interfacial Area Transport Equation) method is employed for water-air two-phase flow to simulate air layers and microbubble mixed flows. For the cavity on the plate bottom, the influence of the front wedge height on air layer wave characteristics is mainly considered. For external conditions, the effects of different incoming flow velocities are primarily considered. The influence of different air injection locations on air layer morphology is also considered, leading to the following conclusions.

The Euler-Euler method combined with the IATE method can achieve numerical simulation of two-phase flow problems related to air layer drag reduction. It can effectively simulate air injection during air layer formation, air-liquid mixing, microbubble flow, and the air-water interface. This provides valuable insights for conducting numerical simulations of model-scale air layer drag reduction ships.

The wave characteristics of the air-water interface on the plate are mainly influenced jointly by the front wedge and the incoming flow velocity. The wave characteristics within the cavity are inherent properties generated by the wedge height and incoming flow velocity. Different wedge heights paired with different incoming flow velocities produce different average wave heights, average wavelengths, and average air layer thicknesses. For the same wedge height, the maximum average air layer thickness corresponds to an optimal incoming flow velocity; velocities that are too low or too high lead to a decrease in average thickness. Simultaneously, under the same incoming flow velocity, different wedge heights also affect the average air layer thickness. As the wedge height increases, the average air layer thickness and average wave height exhibit a trend of first increasing and then decreasing, indicating that for a given incoming flow velocity, there exists an optimal wedge height.The thickest average air layer thickness is obtained at h=0.02 m; lower or higher wedge heights are not conducive to air layer accumulation. This indicates that to achieve the optimal air layer state, the front wedge height must be designed according to the external environmental incoming flow velocity.

The study on air injection location reveals that changing the injection location under the same conditions seems to have little effect on the final stable air layer morphology, only altering the development process of the air layer. However, the influence of air injection rate is not considered in this study, as the research focuses on air layer wave characteristics, requiring a high air flow rate to form the air layer. Nevertheless, in practical applications of air layer drag reduction, the air injection rate is also an important factor affecting drag reduction efficiency. Future research needs to further analyze the impact of changes in air injection rate on drag reduction effectiveness.

ACKNOWLEDGEMENT

This work is supported by the National Natural Science Foundation of China (52131102), to which the authors are most grateful.

REFERENCES

Clark, H, Deutsch, S (1991). “Microbubble skin friction reduction on an axisymmetric body under the influence of applied axial pressure gradients,” *Physics of Fluids*, 3(12), 48–54.

Deutsch, S, Castano, J (1986). “Microbubble skin friction reduction on an axisymmetric body,” *Physics of Fluids*, 29(11), 3590-3597.

Elbing, BR, Solomon, MJ, Perlin, M, et al (2011). “Flow-induced degradation of drag-reducing polymer solutions within a high Reynolds number turbulent boundary layer,” *Journal of Fluid Mechanics*, 670, 337-364.

Gao, QD, Lu, JS, Zhang, GL, Zhang, JW, Wu, WF, Deng, JJ (2023). “Experimental study on bubble drag reduction by the turbulence suppression in bubble flow,” *Ocean Engineering*, 272, 113804.

Ishii, M, Seungjin, K, Joseph, K, (2005). “Development of interfacial area transport equation,” *Nuclear Engineering and Technology*, 7(6), 525-536.

Kodama, Y, Kakugawa, A, Takahashi, T, et al. (2000). “Experimental study on microbubbles and their applicability to ships for skin friction reduction,” *International Journal of Heat and Fluid Flow*, 21, 582-588.

Mccormick, ME, Bhattacharyya, R, (2010). “Drag reduction of a submersible hull by electrolysis,” *Naval Engineers Journal*, 85(2), 11-16.

Menter, FR, (1994). “Two-equation eddy-viscosity turbulence models for engineering applications,” *AIAA*, 32, 1598-605.

Montazeri, M, Alishahi, M (2019). “An efficient method for numerical modeling of thin air layer drag reduction on flat plate and prediction of flow instabilities,” *Ocean Engineering*, 179, 22-37.

Montazeri, M, Alishahi, M (2020). “Investigation of different flow parameters on air layer drag reduction (ALDR) performance using a hybrid stability analysis and numerical solution of the two-phase flow equations,” *Ocean Engineering*, 196, 106779.

Moriguchi, Y, Kato, H (2002). “Influence of microbubble diameter and distribution on frictional resistance reduction,” *Marine Sci. Tech*, 7, 79-85.

Muraia, Y, Fukudab, H, Oishia, Y, Kodama, Y, Yamamoto, F (2007). “Skin friction reduction by large air bubbles in a horizontal channel flow,” *International Journal of Multiphase Flow*, 33(2), 147-163.

Qin, S, Chu, N, Yao, Y, et al (2017). “Stream-wise distribution of skin-friction drag reduction on a flat plate with bubble injection,” *Physics of Fluids*, 29, 037103.

Sato, Y, Sadatomi, M, Sekoguchi, K (1981). “Momentum and heat transfer in two-phase bubble flow—I. Theory.” *Int J Multiphase Flow*, 7(2), 167–177.

Schiller, L, Naumann, AA (1935). “A drag coefficient correlation,” *V.D.I Zeitung*, 77, 318-320.

Sindagi, S, Vijayakumar, R (2021). “Succinct review of MBDR/BDR technique in reducing ship’s drag,” *Ships and Offshore Structures*, 16(9), 968-979.

Takahashi, T, Kakugawa, A, Makino, M, Kodama, Y (2003). “Experimental study on scale effect of drag reduction by microbubbles using very large flat plate ships,” *Journal of the Kansai Society of Naval Architects*, 239, 11-20.

Wang, H, Wang, K, Liu, G (2022). “Drag reduction by gas lubrication with bubbles,” *Ocean engineering*, 258, 1-14.

Winkel, ES (2007). “High Reynolds number flat plate turbulent boundary layer measurements and skin friction drag reduction with gas or polymer injection,” Doctoral dissertation, University of Michigan.